Scientific Research Publishing

Engineering, 2026, 18(6), 197-221
https://www.scirp.org/journal/eng
ISSN Online: 1947-394X
ISSN Print: 1947-3931

Robust Speed Control of SPMSM Drives for EMA Applications Using FACI-STSMC-SMESO-KF

Ehab Alsulami, Yusuf Alturki, Khaled Alnefaie

Department of Electrical and Computer Engineering, Faculty of Engineering, King Abdulaziz University, Jeddah, Saudi Arabia
Email: ehabalsulami@hotmail.com

How to cite this paper: Alsulami, E., Alturki, Y. and Alnefaie, K. (2026) Robust Speed Control of SPMSM Drives for EMA Applications Using FACI-STSMC-SMESO-KF. *Engineering*, **18**, 197-221.
https://doi.org/10.4236/eng.2026.186013

Received: April 3, 2026
Accepted: June 23, 2026
Published: June 26, 2026

Abstract

In this paper, a novel robust nonlinear speed control technique is proposed for EMA-oriented SPMSM drives. Under harsh operating conditions, including unexpected torque disturbances, parameter uncertainties and unmodeled actuator-side effects, current limiter activation, and speed reversal through the zero-speed region, the controller is required to provide precise speed tracking and strong load disturbance rejection. To achieve this objective, an intelligent FACI-STSMC control scheme integrated with an SMESO-KF fusion estimator is developed. A conditional integral term is incorporated into the sliding surface to eliminate the steady-state speed error while avoiding excessive integral accumulation, integrator windup, and transient overshoot. The super-twisting control gains are adaptively tuned through a fuzzy logic algorithm, which suppresses chattering effects while preserving the disturbance rejection capability of the system. In addition, the SMESO reconstructs the total lumped disturbance acting on the speed loop, while the Kalman-filter-based fusion estimator provides a clean and reliable disturbance estimate for speed control. To improve practical implementation, anti-windup current limitation and zero-speed reversal hold-off mechanisms are also introduced. MATLAB/Simulink simulation results validate the effectiveness of the proposed approach, demonstrating improved robustness against parameter uncertainties and unmodeled actuator-side effects, enhanced disturbance rejection, and stable closed-loop performance under demanding EMA operating conditions compared to conventional PI and classical sliding mode controllers.

Keywords

Adaptive Control, Disturbance Rejection, Electro-Mechanical Actuator, Sliding Mode Control, Surface-Mounted Permanent Magnet Synchronous Motor

1. Introduction

The Surface Mounted Permanent Magnet Synchronous Motor (SPMSM) has been identified as one of the most efficient electric drive motors available on account of its excellent power density, high efficiency, small size, and rapid torque response capabilities. This makes it ideal for use in applications, such as the aerospace industry, military, and various industrial operations, particularly EMAs that demand speed control and dynamic performance [1]-[4]. From a control design perspective, the mechanical loads associated with an EMA system appear as complex, time-varying disturbances acting on the SPMSM shaft. In practical operating conditions, these actuators experience sudden load torque changes, parameter variations, such as shifts in stator resistance and inductance, nonlinear friction effects, inverter current saturation, sensor noise, and zero-speed reversal transitions. These factors collectively degrade the speed tracking performance of conventional linear controllers and motivate the development of advanced nonlinear control strategies [2]-[4].

The Field-Oriented Control (FOC) is a widely used control scheme for SPMSM motor drive system which works on the principle of conversion of the nonlinear three-phase quantities into the synchronous rotating reference axis, which permits the control of the d-axis flux-producing current component and the q-axis torque-producing current component separately [5]-[7]. The traditional cascade-type FOC system consists of inner loops of current control of the d-axis and q-axis currents, and the outer speed loop provides the q-axis reference current input. The most commonly utilized controller in the outer speed loop for its simplicity in design, easy tuning, and robustness is the PI controller. However, the PI-based control technique has several drawbacks such as susceptibility to parameter changes and disturbances when dealing with sudden changes in shaft load and nonlinearities in actuator behavior.

Sliding Mode Control (SMC) is widely recognized as a robust control strategy for speed regulation and is often considered an effective alternative to conventional PI-based controllers. The primary benefit of this approach is due to its immunity to uncertainty in matched parameters and bounded external disturbances. Nevertheless, the primary disadvantage of first-order SMC is the effect of chattering caused by the signum function in the feedback controller. In high precision SPMSM-driven EMA, chattering poses a significant issue because it causes ripples in the current flow, resulting in vibrations in the motor and producing extra stresses on the gear train. As a result, it can shorten the lifetime of drive components and degrade the overall control performance. To overcome the trade-off between robustness and control-signal continuity, several higher-order sliding mode control techniques have been developed. Among them, the second-order Super-Twisting Sliding Mode Control (STSMC) algorithm is regarded as one of the most suitable approaches. It generates a continuous control output through an integral-based structure while preserving the robustness and disturbance rejection capability of sliding mode control methods [8]-[13].

In recent years, several advanced nonlinear speed-regulation strategies have been investigated to improve the robustness and dynamic performance of PMSM drives. For example, a super-twisting sliding mode control integrated with a disturbance observer was presented in [12] to enhance disturbance rejection under matched uncertainties. However, high observer or control gains may increase sensitivity to measurement noise and generate oscillatory feedback signals. Similarly, a variable-gain fractional-order super-twisting control method was proposed in [13] to reduce chattering and improve robustness, but the observer structure still depends on deterministic disturbance-bound assumptions. Cascaded extended state observer-based control was also developed in [14] to estimate lumped uncertainties more effectively; nevertheless, high-bandwidth observer structures may introduce noise sensitivity during steady-state operation. In this regard, Kalman-filter-based speed estimation methods, such as the Kalman filter series algorithm [15] and robust adaptive EKF techniques [16], provide improved noise attenuation; however, they may exhibit slower transient response during sudden load variations. Compared with these existing methods, the proposed FACI-STSMC-SMESO-KF controller combines a conditional-integral sliding surface, fuzzy adaptive super-twisting control, SMESO-based disturbance estimation, and Kalman-based fusion within a unified speed-control framework. This integrated structure is designed to balance fast disturbance rejection, reduced chattering, smoother estimation, current-limited operation, and speed reversal robustness for SPMSM-driven EMA applications.

To address the above challenges, this study introduces a Fuzzy Adaptive Conditional-Integral Super-Twisting Sliding Mode Controller with an SMESO-Kalman Fusion Observer (FACI-STSMC-SMESO-KF) for robust speed control of SPMSM-based EMAs. The main contributions of this study are as follows:

- A nonlinear conditional-integral sliding surface is developed that activates error integration only within a defined boundary region, which eliminates steady-state offset while avoiding integrator wind-up and overshoot during large reference speed changes.
- A Sugeno-type fuzzy logic system is incorporated to adjust the super-twisting control gains in real time, providing an online balance between chattering suppression and fast disturbance rejection.
- An SMESO-Kalman fusion observer is designed in which the innovation signal determines how much weight is given to the SMESO estimate versus the Kalman estimate, combining the disturbance tracking strength of the SMESO with the noise rejection capability of the Kalman filter.
- Practical protection features are included, consisting of dynamic anti-windup current limiting and zero-speed reversal hold-off logic, to keep the drive system within safe operating limits at all times.

The suggested control structure is validated in MATLAB/Simulink under a wide range of operating conditions including speed transients, load disturbances, and current saturation. Comparative results against conventional PI-based FOC

and first-order SMC confirm that the proposed FACI-STSMC-SMESO-KF controller achieves better tracking accuracy, lower speed droop, smoother q-axis current behavior, and stable closed-loop operation under severe disturbance conditions.

2. SPMSM-Driven EMA System Modeling

2.1. Electrical Dynamics in the Synchronous *d-q* Reference Frame

By applying the Park transformation to the balanced three-phase stator variables, the SPMSM voltage equations can be expressed in the synchronous rotating *d-q* reference frame as [5]-[7]:

$$v_d = R_s i_d + L_s \frac{\mathrm{d}i_d}{\mathrm{d}t} - \omega_e L_s i_q \tag{1}$$

$$v_q = R_s i_q + L_s \frac{\mathrm{d}i_q}{\mathrm{d}t} + \omega_e L_s i_d + \omega_e \psi_f \tag{2}$$

where v_d and v_q are the *d*-axis and *q*-axis stator voltages, i_d and i_q are the *d*-axis and *q*-axis stator currents, R_s is the stator resistance, L_s is the stator inductance, ω_e is the electrical angular speed, and ψ_f is the permanent magnet flux linkage.

For an SPMSM, the direct-axis and quadrature-axis inductances are approximately equal due to the uniform air-gap reluctance:

$$L_d = L_q = L_s \tag{3}$$

The electromagnetic torque of a PMSM is generally expressed as:

$$T_e = \frac{3}{2} p \left[\psi_f i_q + \left(L_d - L_q \right) i_d i_q \right] \tag{4}$$

where p is the number of pole pairs. Since $L_d = L_q$ for an SPMSM, the reluctance torque component becomes negligible. Therefore, the torque equation is simplified as:

$$T_e = \frac{3}{2} p \psi_f i_q \tag{5}$$

This relation shows that the electromagnetic torque is mainly controlled by the *q*-axis current. Therefore, the commonly adopted FOC strategy sets the *d*-axis current reference to zero:

$$i_d^* = 0 \tag{6}$$

2.2. Mechanical Dynamics and Lumped Disturbance Representation

The actuator-side mechanical dynamics are reflected to the motor shaft and represented using an equivalent mechanical model. This representation is commonly used in motor-drive and EMA control studies, where the actuator-side load, friction, inertia, and unmodeled effects are included in the motor speed dynamics

[2]-[4] [17] [18]. The mechanical speed dynamics can be written as:

$$J_{eq}\frac{\mathrm{d}\omega_m}{\mathrm{d}t} = T_e - B_{eq}\omega_m - T_{L,eq} - T_d \tag{7}$$

where ω_m is the mechanical angular speed, J_{eq} is the equivalent inertia of the motor-actuator system, B_{eq} is the equivalent viscous friction coefficient, $T_{L,eq}$ is the equivalent load torque reflected to the motor shaft, and T_d represents lumped unmodeled disturbances, including nonlinear friction, transmission losses, backlash, compliance, and other actuator-related uncertainties.

Since the electrical and mechanical speeds are related by:

$$\omega_e = p\omega_m \tag{8}$$

The electrical speed dynamics can be derived from the mechanical torque balance and the SPMSM electromagnetic torque equation [5]-[7] as:

$$\frac{\mathrm{d}\omega_e}{\mathrm{d}t} = \frac{3p^2\psi_f}{2J_{eq}}i_q - \frac{B_{eq}}{J_{eq}}\omega_e - \frac{p}{J_{eq}}T_{L,eq} - \frac{p}{J_{eq}}T_d \tag{9}$$

For controller and observer design, the uncertain load and actuator-related effects are grouped into a lumped disturbance term. This lumped-disturbance representation is widely used in observer-based PMSM speed-control systems to simplify disturbance estimation and compensation [12]-[14]. Therefore, the electrical speed dynamics can be rewritten as:

$$\frac{\mathrm{d}\omega_e}{\mathrm{d}t} = K_\omega i_q - \frac{B_{eq}}{J_{eq}}\omega_e + f(t) \tag{10}$$

where

$$K_\omega = \frac{3p^2\psi_f}{2J_{eq}} \tag{11}$$

and $f(t)$ represents the total lumped disturbance. It includes the effects of load torque variation, unmodeled mechanical disturbances, and parameter uncertainties. The lumped disturbance can be expressed as:

$$f(t) = -\Delta K_\omega i_q - \Delta\left(\frac{B_{eq}}{J_{eq}}\right)\omega_e - \frac{p}{J_{eq}}T_{L,eq} - \frac{p}{J_{eq}}T_d \tag{12}$$

where ΔK_ω and $\Delta\left(B_{eq}/J_{eq}\right)$ denote parameter deviations caused by modeling uncertainty, thermal variation, or mechanical changes. The control-oriented model in (10) is suitable for the design of the proposed FACI-STSMC-SMESO-KF controller because it directly relates the control input to the speed dynamics while grouping unknown actuator-side effects into a single disturbance term [12]-[14].

As shown in **Figure 1**, the SPMSM is considered as the electric drive of the EMA system, while the actuator-side mechanical effects are represented by equivalent inertia, viscous friction, reflected load torque, and lumped disturbances acting on the motor shaft.

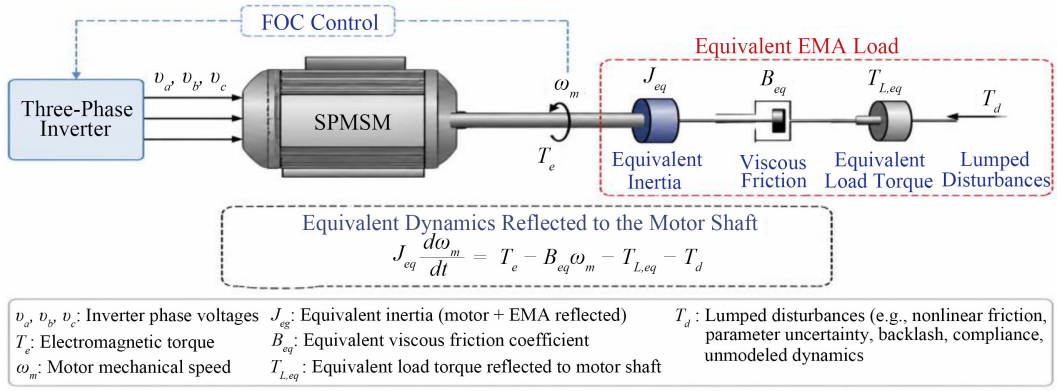

Figure 1. Equivalent motor-control representation of the SPMSM-driven EMA system.

3. Design of the Proposed FACI-STSMC-SMESO-KF Controller

3.1. Overall Control Structure

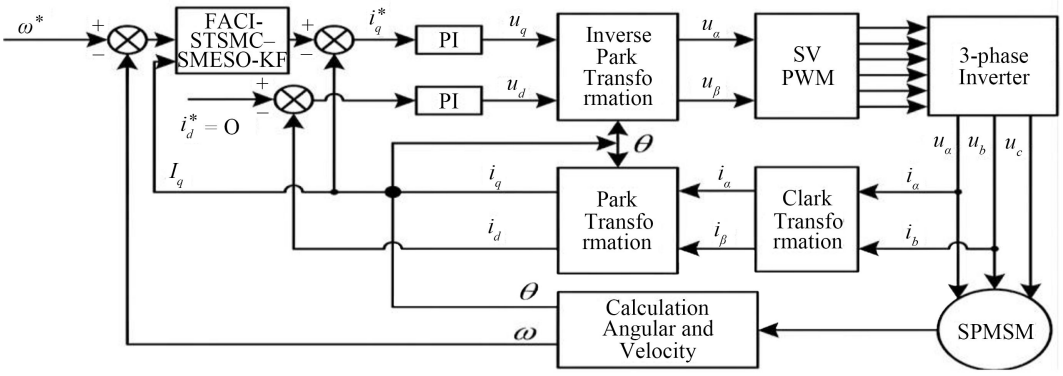

Figure 2. Overall block diagram of the proposed FACI-STSMC-SMESO-KF control structure.

Within the cascaded FOC framework, the proposed FACI-STSMC-SMESO-KF controller serves as the outer speed loop, producing the reference q-axis current command that is tracked by the inner d-axis and q-axis current regulators [5]-[7] [19] [20]. The objective of the designed controller is to achieve accurate speed tracking, disturbance rejection, chattering reduction, and robust performance under practical EMA operating conditions, including abrupt load-torque variations, sensor noise, inverter current saturation, and speed reversal around the zero-speed region [2]-[4] [17] [18]. These requirements are addressed through a control structure composed of four primary components. The integral-type sliding surface reduces the steady-state tracking error by accumulating the speed error, while the conditional integration mechanism mitigates excessive integral action during large transients and inverter current saturation. Furthermore, the super-twisting technique combined with the fuzzy adaptive controller provides continuous higher-order sliding-mode control with online gain adaptation. The SMESO module estimates the total lumped disturbance affecting the speed dynamics, whereas the Kalman filter provides smoothed feedback signals for control purposes [12]-[16]. As shown in **Figure 2**, the proposed FACI-STSMC-SMESO-KF

control structure is implemented within the cascaded field-oriented control framework. The outer speed-control loop generates the reference *q*-axis current command, while the inner current-control loops regulate the *d*-axis and *q*-axis currents.

3.2. Conditional-Integral Sliding Surface

The speed tracking error is defined as:

$$e_{\omega}(t) = \omega_d(t) - \omega_c(t) \tag{13}$$

where $\omega_d(t)$ is the reference speed and $\omega_c(t)$ is the measured motor speed.

The proposed sliding surface is selected as:

$$s(t) = c_s e_{\omega}(t) + c_i e_{int}(t) - K_d \dot{\omega}_{cf}(t) \tag{14}$$

where $s(t)$ is the sliding variable, $c_s > 0$ is the speed-error gain, $c_i > 0$ is the conditional integral gain, $e_{int}(t)$ is the conditional integral error, $K_d > 0$ is the derivative damping coefficient, and $\dot{\omega}_{cf}(t)$ is the filtered speed derivative.

To reduce steady-state tracking error without excessive integral accumulation during large speed transitions, the conditional integral term is activated only when the speed error is inside a predefined boundary region:

$$e_{int}(t) = \begin{cases} \int e_{\omega}(t)\mathrm{d}t, & |e_{\omega}(t)| < E_{int,zone} \\ 0, & |e_{\omega}(t)| \geq E_{int,zone} \end{cases} \tag{15}$$

where $E_{int,zone}$ is the integral activation boundary. This mechanism limits integrator windup and helps reduce transient overshoot during sudden reference speed changes.

3.3. Fuzzy Adaptive Super-Twisting Control Law

The super-twisting sliding mode controller is used to improve robustness while reducing the chattering associated with conventional first-order SMC [8]-[13]. Since the performance of the super-twisting controller depends strongly on its gain, a fuzzy adaptive mechanism is introduced to tune the effective gain online.

The normalized speed error and normalized filtered speed derivative are defined as:

$$E_n = \frac{|e_{\omega}|}{E_{max}} \tag{16}$$

$$DE_n = \frac{|\dot{w}_{cf}|}{DE_{max}} \tag{17}$$

where E_{max} and DE_{max} are normalization constants.

The fuzzy inference system generates a normalized output y_f, which is used to calculate the raw super-twisting gain:

$$K_{st,raw} = K_{st,min} + y_f\left(K_{st,max} - K_{st,min}\right) \tag{18}$$

where $K_{st,min}$ and $K_{st,max}$ are the minimum and maximum allowable super-

twisting gains.

To avoid abrupt gain variation, the effective super-twisting gain is rate-limited as:

$$K_{st,eff}(k) = K_{st,eff}(k-1) + \text{sat}\left(K_{st,raw}(k) - K_{st,eff}(k-1), -\Delta K_{st,max}, \Delta K_{st,max}\right) \quad (19)$$

where $\Delta K_{st,max}$ is the maximum allowable gain change per sampling interval.

The first super-twisting term is defined as:

$$u_1(t) = \sqrt{K_{st,eff}}\sqrt{|s(t)|} + \varepsilon\,\text{sat}\left(\frac{s(t)}{e_{c,s}}\right) \quad (20)$$

where ε is a small positive constant used to avoid numerical singularity, and $e_{c,s}$ is the sliding-surface boundary-layer width.

The second super-twisting term is updated as:

$$\dot{u}_2(t) = \lambda_{st} K_{st,eff}\,\text{sat}\left(\frac{s(t)}{e_{c,s}}\right) - \ell(t)u_2(t) \quad (21)$$

where $\lambda_{st} > 0$ is a design coefficient and $\ell(t)$ is a leakage coefficient used to limit excessive accumulation in the integral robust term.

The total super-twisting control signal is given by:

$$u_s(t) = u_1(t) + u_2(t) \quad (22)$$

The unsaturated q-axis current command is then obtained as:

$$i_{q,unsat}^{*} = u_s(t) \quad (23)$$

This structure provides a continuous higher-order sliding control action, which improves chattering behavior while maintaining robustness against bounded disturbances [8]-[13].

3.4. SMESO-Kalman Fusion Observer

The Sliding-Mode Extended State Observer is used to estimate the speed-related states and the lumped disturbance. The observer states are defined as:

$$\hat{x}_1 = \hat{\omega}_{pu} \quad (24)$$

$$\hat{x}_2 = \hat{\dot{\omega}}_{pu} \quad (25)$$

$$\hat{x}_3 = \hat{d}_{pu} \quad (26)$$

where $\hat{x}_1$ is the estimated speed, $\hat{x}_2$ is the estimated speed derivative, and $\hat{x}_3$ is the estimated lumped disturbance.

The observer error is defined as:

$$e_o = \omega_{pu} - \hat{x}_1 \quad (27)$$

The SMESO dynamics are expressed as:

$$\dot{\hat{x}}_1 = \hat{x}_2 + \beta_1 e_o \quad (28)$$

$$\dot{\hat{x}}_2 = -a\hat{x}_1 + b\left(i_q + \hat{x}_3\right) + \beta_2\,\text{sat}\left(\frac{e_o}{e_{c,o}}\right) \quad (29)$$

$$\dot{\hat{x}}_3 = \beta_3 \,\mathrm{sat}\left(\frac{e_o}{e_{c,o}}\right) \tag{30}$$

where β_1, β_2, and β_3 are the observer gains, and $e_{c,o}$ is the observer boundary-layer width. The saturation function is used to reduce noise amplification in the observer dynamics. The SMESO gains are selected based on the observer bandwidth Λ and the observer boundary-layer width $e_{c,o}$, such that $\beta_1 = l_{1o}$, $\beta_2 = l_{2o}$, and $\beta_3 = l_{3o}$, where $l_{1o} = 3\Lambda e_{c,o}$, $l_{2o} = 3\Lambda^2 e_{c,o}$, and $l_{3o} = \Lambda^3 e_{c,o}$. These gain factors are kept fixed throughout the simulation study. To improve estimation smoothness, a Kalman filter is incorporated as an auxiliary estimation layer. The Kalman filter state vector is defined as:

$$\boldsymbol{x}_{KF}(k) = \begin{bmatrix} \hat{\omega}_{KF}(k) \\ \hat{\dot{\omega}}_{KF}(k) \\ \hat{d}_{KF}(k) \end{bmatrix} \tag{31}$$

The Kalman filter is formulated using a discrete-time prediction and correction structure. The state vector consists of the estimated speed, estimated acceleration, and estimated lumped disturbance, as defined in (31). The prediction model is expressed as:

$$\boldsymbol{x}_{KF}^{-}(k) = \boldsymbol{A}_{KF}\boldsymbol{x}_{KF}(k-1) + \boldsymbol{B}_{KF} i_q(k-1) \tag{32}$$

$$\boldsymbol{P}^{-}(k) = \boldsymbol{A}_{KF}\boldsymbol{P}(k-1)\boldsymbol{A}_{KF}^{\mathrm{T}} + \boldsymbol{Q} \tag{33}$$

where $\boldsymbol{x}_{KF}^{-}(k)$ is the predicted state vector, $\boldsymbol{P}^{-}(k)$ is the predicted error covariance matrix, $\boldsymbol{A}_{KF}$ is the discrete-time state transition matrix, $\boldsymbol{B}_{KF}$ is the input matrix, $i_q(k-1)$ is the previous q-axis current input, and $\boldsymbol{Q}$ is the process noise covariance matrix. The measurement equation is given by:

$$y(k) = \boldsymbol{C}_{KF}\boldsymbol{x}_{KF}(k) + v(k) \tag{34}$$

where $y(k)$ is the measured speed, $\boldsymbol{C}_{KF}$ is the measurement matrix, and $v(k)$ is the measurement noise. The measurement noise covariance is denoted by $\boldsymbol{R}$.

The Kalman gain is calculated as:

$$\boldsymbol{K}_{KF}(k) = \boldsymbol{P}^{-}(k)\boldsymbol{C}_{KF}^{\mathrm{T}}\left[\boldsymbol{C}_{KF}\boldsymbol{P}^{-}(k)\boldsymbol{C}_{KF}^{\mathrm{T}} + \boldsymbol{R}\right]^{-1} \tag{35}$$

The corrected state and covariance are then updated as:

$$\boldsymbol{x}_{KF}(k) = \boldsymbol{x}_{KF}^{-}(k) + \boldsymbol{K}_{KF}(k)\left[y(k) - \boldsymbol{C}_{KF}\boldsymbol{x}_{KF}^{-}(k)\right] \tag{36}$$

$$\boldsymbol{P}(k) = \left[\boldsymbol{I} - \boldsymbol{K}_{KF}(k)\boldsymbol{C}_{KF}\right]\boldsymbol{P}^{-}(k) \tag{37}$$

In this work, the process noise covariance matrix is selected as:

$$\boldsymbol{Q} = \mathrm{diag}\left(q_\omega, q_{\dot{\omega}}, q_d\right) \tag{38}$$

where q_ω, $q_{\dot{\omega}}$, and q_d represent the process noise levels associated with the speed, acceleration, and disturbance states, respectively. The measurement noise covariance is denoted by $\boldsymbol{R}$. The numerical values of $\boldsymbol{Q}$ and $\boldsymbol{R}$ are selected as part of the Kalman observer tuning parameters used in the simulation study.

The Kalman filter is initialized using the measured initial speed, while the initial acceleration and disturbance states are set to zero. The initial covariance matrix is selected as a diagonal positive-definite matrix to allow the estimator to converge during the initial transient period.

The disturbance-related state is generated by treating the lumped disturbance as an augmented slowly varying state. This allows the Kalman filter to smooth the disturbance estimate while the SMESO provides fast disturbance-sensitive estimation. The innovation signal is then used to determine the fusion weighting between the Kalman estimate and the SMESO estimate.

The innovation signal is defined as:

$$r(k) = y(k) - \boldsymbol{C}_{KF}\boldsymbol{x}_{KF}^{-}(k) \tag{39}$$

where $y(k)$ is the measured speed and $\boldsymbol{x}_{KF}^{-}(k)$ is the predicted Kalman state vector. The absolute innovation is:

$$r_a(k) = |r(k)| \tag{40}$$

The fusion weight is calculated as:

$$\alpha_f(k) = \mathrm{sat}\left(\frac{r_a(k) - r_0}{r_1 - r_0}, 0, 1\right) \tag{41}$$

where r_0 and r_1 are the lower and upper innovation thresholds. The fused speed estimate is expressed as:

$$\hat{\omega}_{fused}(k) = \alpha_f(k)\hat{\omega}_{KF}(k) + \left(1 - \alpha_f(k)\right)\hat{\omega}_{SMESO}(k) \tag{42}$$

The fused disturbance estimate is:

$$\hat{d}_{fused}(k) = \alpha_f(k)\hat{d}_{KF}(k) + \left(1 - \alpha_f(k)\right)\hat{d}_{SMESO}(k) \tag{43}$$

The Kalman filter provides smooth estimation during normal operation, while the SMESO improves robustness during sudden disturbances. Therefore, the innovation-based fusion mechanism combines the advantages of both estimators to improve feedback reliability [12] [16].

3.5. Final Current Command and Practical Protection

The fused disturbance estimate is then incorporated into the super-twisting current command to provide active load compensation:

$$i_{q,cmd}^{*} = i_{q,unsat}^{*} - \alpha_{eff}\,\hat{d}_{fused} \tag{44}$$

where α_{eff} is the effective disturbance compensation gain.

During reversal hold-off or near-current-saturation conditions, the disturbance compensation term is restricted to avoid excessive current demand or unstable compensation:

$$i_{q,cmd}^{*} = \begin{cases} i_{q,unsat}^{*}, & \sigma_{hold} = 1 \text{ or } \left|i_{q,prev}^{*}\right| \geq 0.98\, i_{q,max} \\ i_{q,unsat}^{*} - \alpha_{eff}\,\hat{d}_{fused}, & \end{cases} \tag{45}$$

The final q-axis current command is limited within the allowable current range:

$$i_{q,ref}^{*} = \mathrm{sat}\left(i_{q,cmd}^{*}, i_{q,min}, i_{q,max}\right) \tag{46}$$

where $i_{q,min}$ and $i_{q,max}$ are the allowable q-axis current limits.

During fast load-recovery operation, an additional feedforward current term is added:

$$i_{q,ref}^{*} = \mathrm{sat}\left(i_{q,cmd}^{*} + i_{q,ff}^{*}, i_{q,min}, i_{q,max}\right) \tag{47}$$

where $i_{q,ff}^{*}$ is the feedforward current calculated from the estimated load torque. This practical protection structure improves disturbance recovery while keeping the current command within the safe operating limits of the inverter and motor.

3.6. Stability Analysis of the Proposed FACI-STSMC-SMESO-KF Controller

Before presenting the Lyapunov-based stability analysis, the following assumptions are considered. First, the reference speed $\omega_d(t)$ and its derivative are assumed to be bounded. Second, the lumped disturbance $d(t)$, which includes load torque variation, friction effects, parameter uncertainties, and unmodeled actuator-side dynamics, is assumed to be bounded. Third, the disturbance estimation error produced by the SMESO-Kalman fusion observer is assumed to remain bounded. Fourth, all controller gains, including the sliding surface gains and the effective super-twisting gain, are selected as positive finite constants. Fifth, the q-axis current command is bounded by the imposed current saturation limits. Finally, the saturation functions used in the controller and observer introduce finite boundary layers to reduce chattering and noise amplification.

Under these assumptions, the proposed controller is analyzed in terms of practical bounded convergence. Therefore, the objective of the stability analysis is not to prove ideal global asymptotic stability, but to show that the sliding variable converges to a bounded neighborhood around the origin under bounded disturbance, observer-error, and current-limited operating conditions.

A Lyapunov-based stability analysis is presented to evaluate the convergence behavior of the proposed FACI-STSMC-SMESO-KF controller. The analysis focuses on the sliding variable defined in (14). Since the proposed controller is based on a super-twisting sliding mode structure, the reaching condition is examined using the selected Lyapunov candidate function [8]-[13].

The Lyapunov candidate function is selected as:

$$V(t) = \frac{1}{2}s^{2}(t) \tag{48}$$

where $s(t)$ is the sliding variable. The function $V(t)$ is positive definite for $s(t) \neq 0$ and becomes zero when $s(t) = 0$. Taking the time derivative of (48) gives:

$$\dot{V}(t) = s(t)\dot{s}(t) \tag{49}$$

For sliding mode control, the reaching condition requires that the sliding variable and its derivative have opposite signs. Therefore, the stability condition can

be written as [8]-[11]:

$$s(t)\dot{s}(t)<0 \tag{50}$$

or equivalently:

$$\dot{V}(t)<0 \tag{51}$$

The proposed controller uses the fused disturbance estimate to compensate for the lumped disturbance. The disturbance estimation error is defined as:

$$\tilde{d}(t)=d(t)-\hat{d}_{fused}(t) \tag{52}$$

where $d(t)$ is the actual lumped disturbance and $\hat{d}_{fused}(t)$ is the disturbance estimate obtained from the SMESO-Kalman fusion observer. Assuming that the lumped disturbance and the estimation error are bounded, the following condition holds:

$$\left|\tilde{d}(t)\right|\le\Delta_d \tag{53}$$

where $\Delta_d>0$ is a bounded positive constant.

Under the proposed fuzzy adaptive super-twisting control law, the effective control gain is adjusted online to dominate the bounded disturbance estimation error. Therefore, the Lyapunov derivative can be bounded as:

$$\dot{V}(t)\le-\eta\left|s(t)\right| \tag{54}$$

where $\eta>0$ is a positive design constant. Since $\dot{V}(t)\le 0$, the Lyapunov function is non-increasing, and the sliding variable is driven toward the sliding surface. This confirms that the reaching condition is satisfied under bounded disturbance and estimation error conditions. Super-twisting sliding mode control is commonly used to improve robustness while reducing the chattering associated with conventional first-order SMC [8]-[13].

In practical implementation, a saturation function is used instead of an ideal discontinuous sign function to reduce chattering in the generated q-axis current command. Therefore, the sliding variable converges to a small boundary layer around the origin:

$$\left|s(t)\right|\le e_{c,s} \tag{55}$$

where $e_{c,s}$ is the sliding-surface boundary-layer width.

When the system trajectory enters this boundary layer, the conditional integral term becomes active and reduces the residual steady-state tracking error. In addition, the SMESO-Kalman fusion observer provides bounded speed and disturbance estimates, while the current saturation and anti-windup mechanisms keep the control input within safe operating limits. Therefore, the proposed FACI-STSMC-SMESO-KF controller achieves practical closed-loop stability under bounded disturbances, estimation errors, and current-limited operating conditions [12]-[16].

It should be noted that the obtained stability result represents practical bounded convergence rather than ideal global asymptotic stability. This is because the im-

plemented controller includes saturation functions, current limits, observer fusion, and protection logic. Nevertheless, the analysis confirms that the proposed controller drives the sliding variable toward a bounded neighborhood around zero while maintaining stable speed tracking behavior.

4. Results and Discussion

4.1. Simulation Setup

The proposed control strategy is evaluated using MATLAB/Simulink. The simulation model is developed based on the SPMSM mathematical model and the EMA-equivalent shaft load representation described in Section 2. The initial simulation structure is based on the Field-Oriented Control framework, where the inner current loops regulate the *d*-axis and q-axis currents, while the outer speed loop generates the reference *q*-axis current command [5]-[7] [19]. The MATLAB/ Simulink implementation is modified from the Motor Control Blockset FOC example to include the proposed FACI-STSMC-SMESO-KF speed controller, SMESO-Kalman fusion observer, current saturation handling, anti-windup action, reversal hold-off logic, and fast load-recovery compensation [20]. **Figure 3** shows the MATLAB/Simulink implementation of the proposed SPMSM drive system. The model includes the SPMSM plant, three-phase voltage source inverter, SVPWM block, coordinate transformations, inner current controllers, outer speed controller, observer structure, and load torque disturbance input.

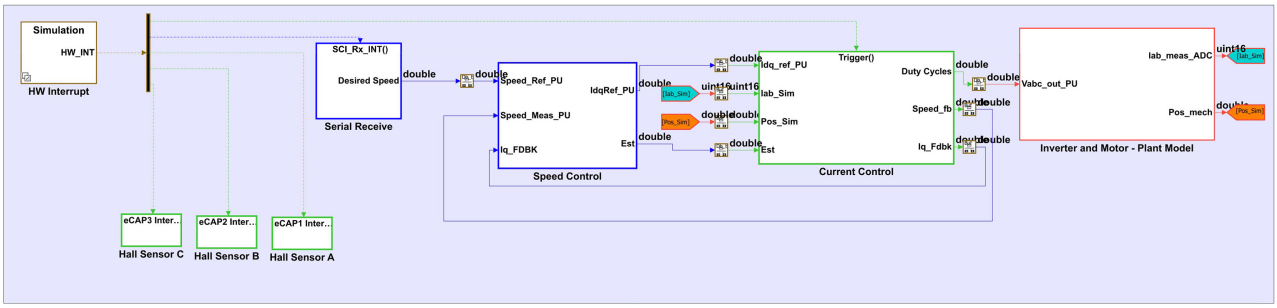

Figure 3. MATLAB/Simulink implementation of the proposed SPMSM drive system.

The main motor parameters, voltage condition, control settings, and load disturbance profile used in the simulation are summarized in **Table 1**. These parameters are used consistently for the PI-based FOC, traditional SMC, and proposed FACI-STSMC-SMESO-KF controllers to ensure a fair comparison under identical operating conditions. In addition, **Tables 2-4** present the tuning parameters of the proposed FACI-STSMC-SMESO-KF controller, the traditional SMC baseline controller, and the PI-based FOC baseline controller, respectively. These tuning tables are included to improve the reproducibility of the simulation study and to clarify the controller, observer, fusion, and protection settings used in the comparative evaluation.

Table 1. SPMSM drive parameters and simulation conditions.

Parameter	Symbol	Value
Number of pole pairs	p	2
Permanent magnet flux linkage	ψ_f	0.0055 Wb
Stator resistance	R_s	0.0825 Ω
d-axis inductance	L_d	0.00018 H
q-axis inductance	L_q	0.00018 H
Equivalent inertia	J	2.104 e^{-5} kg·m^2
Viscous friction coefficient	B	1.0 e^{-5} N·m·s/rad
Base current	I_{base}	30
Base speed	N_{base}	8585
Rated torque	T_{rated}	0.3276
Load disturbance magnitude	T_L	0.1638 N·m
Load disturbance time	t_L	0.3 s
Sampling time	T_s	6.6667e^{-4} s

The parameters listed in Table 1 are used for all simulation cases to ensure a fair comparison between the PI-based FOC, traditional SMC, and proposed FACI-STSMC-SMESO-KF controllers. The load torque disturbance is applied at $t = 0.3\,\text{s}$ with a magnitude of $0.5T_{rated}$, corresponding to 0.1638 N·m. This disturbance represents the EMA-equivalent shaft load applied to the SPMSM and is used to evaluate the disturbance rejection and recovery capability of each controller.

Tables 2-4 summarize the tuning parameters used for the proposed FACI-STSMC-SMESO-KF controller, the traditional SMC baseline controller, and the PI-based FOC baseline controller, respectively. These tables are included to improve the reproducibility of the simulation study and to clarify the controller, observer, fusion, and protection settings used in the comparative evaluation.

Table 2. Proposed FACI-STSMC-SMESO-KF controller and observer tuning parameters.

Subsystem Layer	Tuning Parameter	Symbol	Nominal Value
Conditional-integral sliding surface	Speed error proportional gain	C_s	15.0
Conditional-integral sliding surface	Conditional integral gain	C_i	12.0
Conditional-integral sliding surface	Derivative damping factor	K_d	0.075
Conditional-integral sliding surface	Sliding surface boundary-layer width	$e_{c,s}$	0.45
Conditional-integral sliding surface	Integral activation zone threshold	$E_{int,zone}$	0.01 p.u.
Fuzzy adaptive super-twisting law	Error normalization ceiling	E_{max}	1.0
Fuzzy adaptive super-twisting law	Derivative normalization ceiling	DE_{max}	10.0
Fuzzy adaptive super-twisting law	Minimum baseline super-twisting gain	$K_{st,min}$	1.0
Fuzzy adaptive super-twisting law	Maximum baseline super-twisting gain	$K_{st,max}$	20.0

Continued

Fuzzy adaptive super-twisting law	Nominal gain variation rate limit	$\Delta K_{st,max}$	28 T_s
SMESO layer	Observer tuning bandwidth	Λ	850
SMESO layer	Speed estimation gain factor	l_{1o}	$3\Lambda e_{c,o} = 127.5$
SMESO layer	Acceleration feedback gain factor	l_{2o}	$3\Lambda^2 e_{c,o} = 54{,}187.5$
SMESO layer	Lumped disturbance tracking gain factor	l_{3o}	$\Lambda^3 e_{c,o} = 1.5353 \times 10^7$
SMESO layer	Observer boundary-layer width	$e_{c,o}$	0.05
Kalman observer fusion matrix	Speed state covariance noise	q_ω	5×10^{-3}
Kalman observer fusion matrix	Acceleration state covariance noise	q_ω	5×10^{-3}
Kalman observer fusion matrix	Disturbance state covariance noise	q_d	4×10^{-4}
Kalman observer fusion matrix	Measurement noise covariance scaling	R	1×10^{-4}
Kalman observer fusion matrix	Lower innovation filtering boundary	r_0	0.01
Kalman observer fusion matrix	Upper innovation filtering boundary	r_1	0.06
Hardware constraints and protection	Hard saturation current envelope	$[i_{q,min}, i_{q,max}]$	±1.0 p.u. (±30 A)
Hardware constraints and protection	Forward disturbance compensation scale	α_{eff}	0.08 to 1.0

Table 3. Traditional SMC controller tuning parameters.

Subsystem Layer	Tuning Parameter	Symbol	Nominal Value
Sliding surface	Integral sliding gain	C	0.9
Sliding surface	Integral accumulator limit	int_{lim}	±0.65
Switching function	Boundary-layer width	ϕ	0.05
Switching function	Switching gain	K_s	1.0
Hardware constraints and protection	Hard saturation current envelope	$[i_{q,min}, i_{q,max}]$	±1.0 p.u. (±30 A)

Table 4. PI-Based FOC speed controller tuning parameters.

Subsystem Layer	Tuning Parameter	Symbol	Nominal Value
PI speed controller	Proportional gain	$K_{p,speed}$	4.3
PI speed controller	Integral gain	$K_{i,speed}$	0.057
Hardware constraints and protection	Hard saturation current envelope	$[i_{q,min}, i_{q,max}]$	±1.0 p.u. (±30 A)

The PI-based FOC speed controller was tuned using the baseline speed-loop tuning procedure of the cascaded FOC structure. The proportional gain was first adjusted to obtain a fast speed response without excessive overshoot, and then the integral gain was gradually increased to reduce the steady-state speed error. After achieving an acceptable balance between transient response, overshoot, and steady-state accuracy, the final PI gains were fixed and used for all simulation cases.

The traditional SMC baseline controller was tuned by adjusting the sliding surface gain, integral limitation, switching gain, and boundary-layer width. The sliding surface gain was selected to improve tracking performance, while the integral

limitation was introduced to prevent excessive error accumulation. The switching gain was adjusted to enhance disturbance rejection, and the boundary-layer saturation function was used to reduce high-frequency chattering.

For the proposed FACI-STSMC-SMESO-KF controller, the conditional-integral sliding surface, fuzzy adaptive super-twisting law, SMESO gains, Kalman fusion parameters, and hardware protection settings were tuned iteratively in MATLAB/Simulink. The tuning objective was to achieve fast speed tracking, bounded q-axis current response, reduced chattering, accurate disturbance estimation, and stable compensation under EMA-equivalent shaft load conditions. The final parameters of all controllers were kept constant during the reported simulations. The same SPMSM model, sampling time, current limits, reference speed profile, and load disturbance conditions were used to ensure a fair comparison among the tested controllers.

Before presenting the quantitative comparison, the performance indices used in this study are defined to clarify the evaluation procedure. The tracking error is calculated as:

$$e(t) = \omega_d(t) - \omega_c(t) \tag{56}$$

where $\omega_d(t)$ is the reference speed and $\omega_c(t)$ is the actual motor speed. The root mean square error (RMSE) is used to evaluate the overall tracking accuracy and is defined as:

$$\mathrm{RMSE} = \sqrt{\frac{1}{N}\sum_{k=1}^{N} e^2(k)} \tag{57}$$

The mean absolute error (MAE) is calculated as:

$$\mathrm{MAE} = \frac{1}{N}\sum_{k=1}^{N} \left|e(k)\right| \tag{58}$$

The integral absolute error (IAE) is used to measure the accumulated absolute tracking error over time:

$$\mathrm{IAE} = \int_0^T \left|e(t)\right| \mathrm{d}t \tag{59}$$

The integral time absolute error (ITAE) is defined as:

$$\mathrm{ITAE} = \int_0^T t\left|e(t)\right| \mathrm{d}t \tag{60}$$

The integral square error (ISE) is calculated as:

$$\mathrm{ISE} = \int_0^T e^2(t)\,\mathrm{d}t \tag{61}$$

The final steady-state error is expressed as:

$$\mathrm{SSE}_{\mathrm{end}} = e(T) \tag{62}$$

where T is the end simulation time. In order to compare the results based on steps, the rise time can be considered as the time taken by the speed response from 10% to 90% of the final reference value. The settling time will be the time taken by the speed response to reach and stay in a range ±2% of the final reference value. The

percentage overshoot will be measured relative to the final reference value of each step of speed. The same criteria have been considered while evaluating the performance of the PI-based FOC, conventional SMC, and proposed FACI-STSMC-SMESO-KF systems.

4.2. Speed Tracking, Current Response, and Performance Indices

The dynamic performance of the speed-control loop is evaluated under a multi-step reference speed profile, including a sudden shaft load torque disturbance and a speed reversal condition, as illustrated in Figure 4. At $t = 0.3\,\text{s}$, an external load torque disturbance equal to 50% of the rated torque (0.1638 N·m) is applied to the SPMSM shaft. Under this disturbance condition, the conventional PI-based FOC controller exhibits a noticeable speed droop and a longer recovery interval, while the traditional SMC controller improves disturbance rejection but introduces higher oscillations due to its switching control action. In contrast, the proposed FACI-STSMC-SMESO-KF controller effectively reduces the disturbance effect and restores the speed response rapidly. This improvement is mainly attributed to the combined action of the SMESO-Kalman fusion observer, disturbance compensation, fuzzy adaptive super-twisting control, and current-limited anti-windup mechanism.

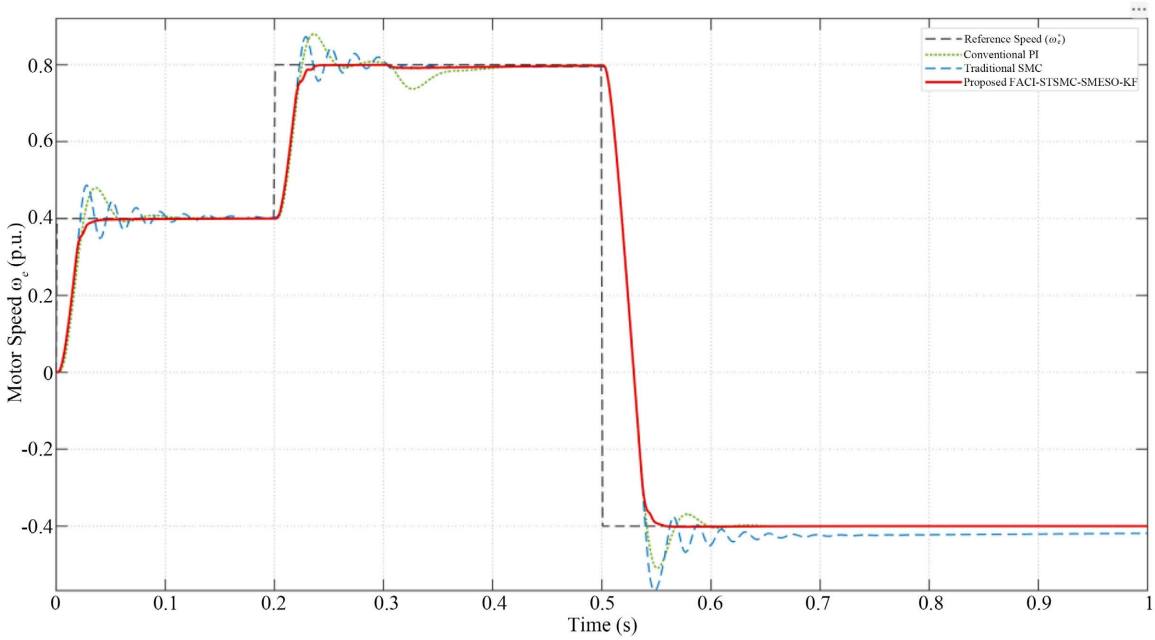

Figure 4. Speed tracking response comparison of PI-based FOC, traditional SMC, and proposed FACI-STSMC-SMESO-KF controller.

Furthermore, to examine the robustness of the proposed controller during direction reversal, a speed reversal command is applied from +0.8 p.u. to −0.4 p.u. at $t = 0.5\,\text{s}$. This operating condition is critical for EMA-oriented drives because the speed trajectory crosses the zero-speed region, where measurement noise, sign changes, and nonlinear load effects may degrade control performance. The PI-

based FOC controller shows larger transient oscillations and slower settling during the reversal interval, while the traditional SMC controller produces stronger current ripple due to its discontinuous switching behavior. The proposed FACI-STSMC-SMESO-KF controller provides smoother zero-speed crossing, lower transient oscillation, and faster stabilization at the negative speed reference. These results confirm that the proposed controller improves speed tracking, disturbance rejection, and reversal robustness under EMA-equivalent operating conditions.

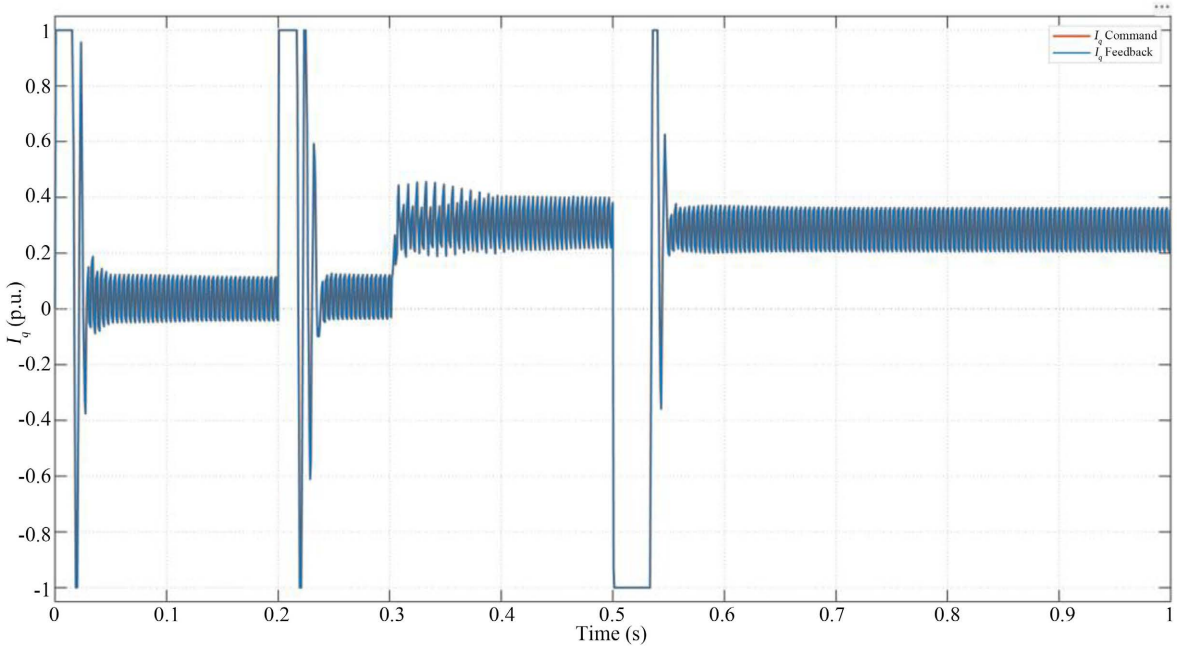

Figure 5. q-axis current response of the proposed FACI-STSMC-SMESO-KF controller.

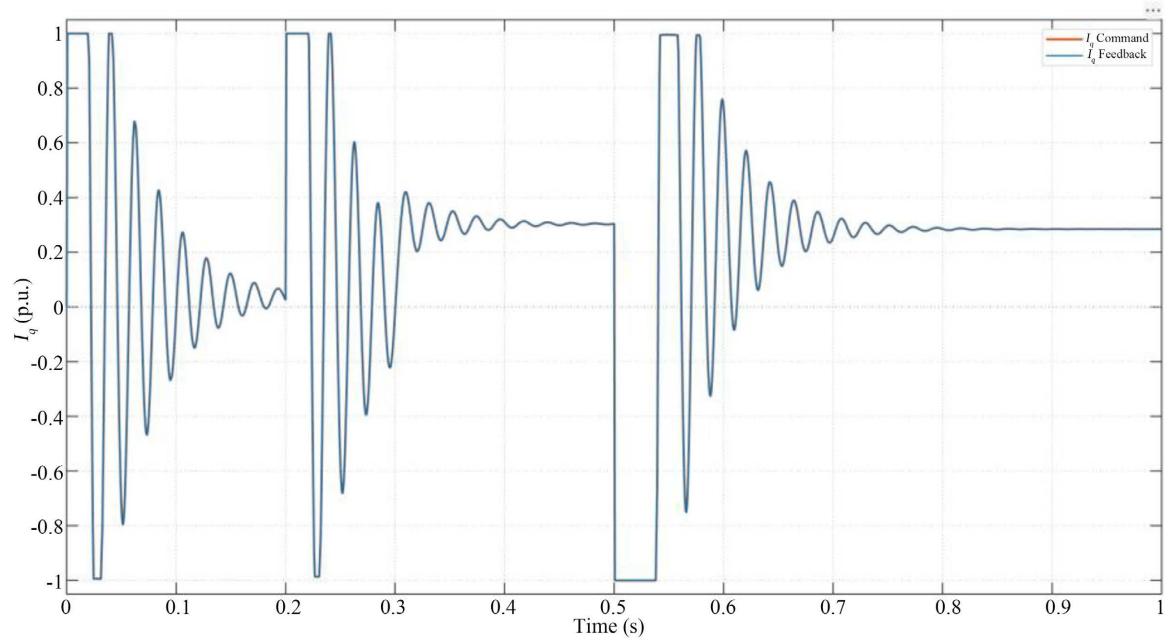

Figure 6. q-axis current response of the traditional SMC controller.

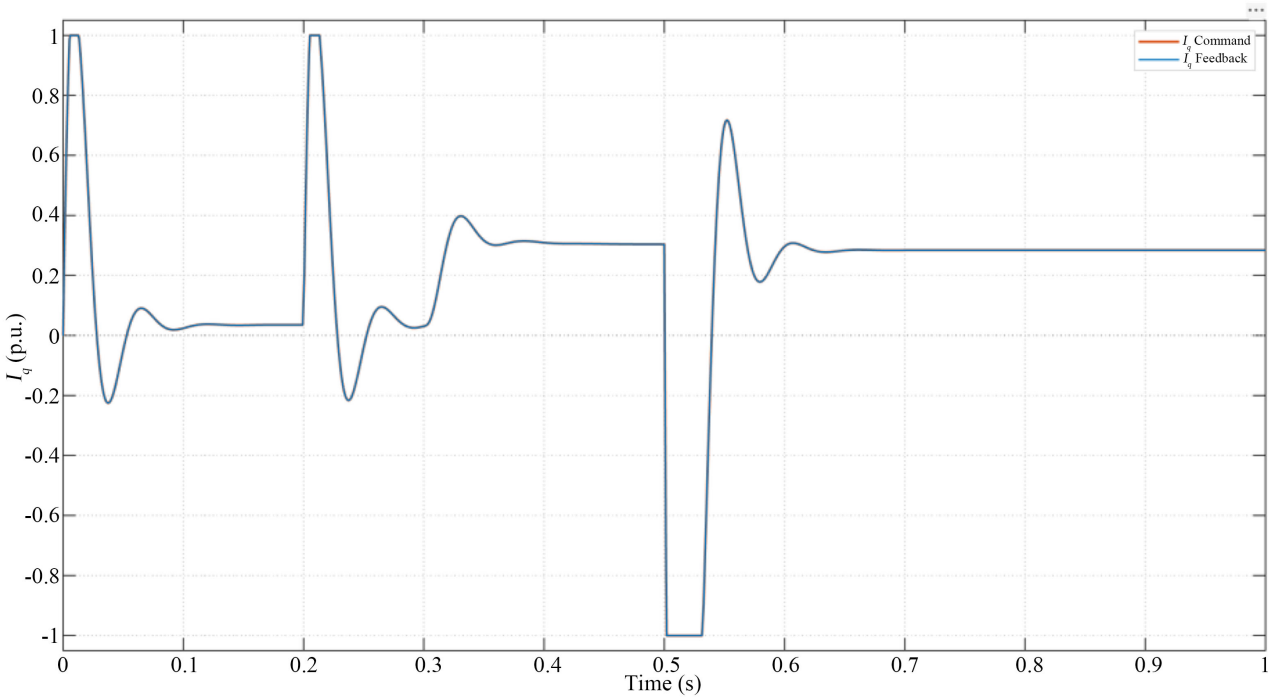

Figure 7. q-axis current response of the PI controller.

Figures 5-7 show the q-axis current responses of the proposed FACI-STSMC-SMESO-KF controller, traditional SMC controller, and PI-based FOC controller, respectively. Since the q-axis current is directly related to the electromagnetic torque of the SPMSM, its response is an important indicator of current smoothness, torque ripple, and practical implementation quality.

The current responses in Figures 5-7 confirm the practical behavior and current-limiting capability of each tested controller under the applied operating conditions. The proposed FACI-STSMC-SMESO-KF controller in Figure 5 maintains a bounded and smoother q-axis current response during rapid speed transitions and external load disturbance conditions. During the acceleration intervals and the speed reversal event at $t = 0.5\,\mathrm{s}$, the reference q-axis current reaches the imposed physical limits of ±1.0 p.u. The integrated current limitation and anti-windup mechanism help prevent excessive integral accumulation and support smooth recovery after saturation.

In contrast, the traditional SMC controller in Figure 6 exhibits more noticeable high-frequency current oscillations due to the switching nature of the discontinuous control law. These oscillations may increase torque ripple and mechanical stress in practical SPMSM-driven EMA systems. Meanwhile, the PI-based FOC controller in Figure 7 requires a larger corrective current during transient recovery intervals and shows slower current settling under load disturbance and speed reversal conditions. Therefore, the proposed controller provides a better compromise between fast load disturbance rejection, current smoothness, and safe torque-producing current generation.

Table 5. Overall performance comparison of the tested controllers.

Performance Index	PI	SMC	FACI-STSMC-SMESO-KF
RMSE	0.1724	0.1700	0.1688
MAE	0.0493	0.0564	0.0413
IAE	0.0493	0.0565	0.0414
ITAE	0.0187	0.0255	0.0163
ISE	0.0298	0.0289	0.0285
SSE_{end}	8.8655e−06	0.0189	−1.0661e−04

The overall performance comparison in Table 5 shows that the proposed FACI-STSMC-SMESO-KF controller achieves the best tracking performance among the tested controllers. Compared with the PI-based FOC and traditional SMC controllers, the proposed controller provides the lowest RMSE, MAE, IAE, ITAE, and ISE values. This confirms that the proposed method improves speed tracking accuracy, reduces accumulated tracking error, and enhances transient performance under reference speed variations and EMA-equivalent shaft load disturbance conditions. Although the final steady-state error remains very small for all controllers, the proposed controller offers the best overall balance between tracking accuracy, disturbance rejection, and smooth dynamic response.

Table 6. Step-based performance comparison of the tested controllers.

Step No.	Controller	Rise Time	Settling Time	Overshoot %	SSE_{end}	RMSE	IAE	ITAE
1	PI-Based FOC	0.0147	0.065333	19.970	-3.20×10^{-4}	0.10166	7.89×10^{-3}	1.42×10^{-4}
1	Traditional SMC	0.0140	0.13867	21.681	-3.11×10^{-3}	0.095008	7.78×10^{-3}	1.95×10^{-4}
1	Proposed FACI-STSMC-SMESO-KF	0.0138	0.034000	0.026034	-7.05×10^{-5}	0.092989	5.88×10^{-3}	6.46×10^{-5}
2	PI-Based FOC	0.0147	0.20333	19.873	8.02×10^{-4}	0.084787	1.07×10^{-2}	5.67×10^{-4}
2	Traditional SMC	0.0153	0.28200	17.601	5.20×10^{-3}	0.076942	8.29×10^{-3}	3.55×10^{-4}
2	Proposed FACI-STSMC-SMESO-KF	0.0145	0.14133	0	2.14×10^{-3}	0.077349	6.98×10^{-3}	2.47×10^{-4}
3	PI-Based FOC	0.02733	0.084000	9.0127	8.87×10^{-6}	0.225980	3.011×10^{-2}	5.32×10^{-4}
3	Traditional SMC	0.02733	0.16600	13.542	1.89×10^{-2}	0.225040	3.97×10^{-2}	3.19×10^{-3}
3	Proposed FACI-STSMC-SMESO-KF	0.02733	0.045333	0	-1.07×10^{-4}	0.223540	2.78×10^{-2}	4.11×10^{-4}

The step-based comparison in Table 6 confirms that the proposed FACI-STSMC-SMESO-KF controller provides the best transient performance among the tested controllers. It achieves significantly lower overshoot and smaller tracking error values compared with the PI-based FOC and traditional SMC controllers. This improvement verifies the effectiveness of the conditional-integral super-twisting control law and the SMESO-Kalman disturbance compensation mechanism under EMA-equivalent shaft load conditions.

4.3. Observer and Load Torque Estimation Results

Figure 8 presents the estimated speed responses obtained using the Kalman filter,

the SMESO, and the proposed SMESO-Kalman fusion estimator. All three estimators are able to track the measured speed response under reference speed variations and load-torque disturbance conditions. However, the estimated speed responses exhibit different characteristics in terms of transient response, noise attenuation, and signal smoothness.

The Kalman filter provides a smooth speed estimate during steady-state operation due to its stochastic filtering nature. However, its transient response may be relatively slow during rapid speed variations and sudden load disturbances. In contrast, the SMESO-based speed estimate responds faster to disturbance changes, but it may contain higher oscillations due to the sliding-mode correction action.

The proposed SMESO-Kalman fusion estimator combines the advantages of both methods by utilizing the fast disturbance-sensitive response of the SMESO and the smoothing capability of the Kalman filter. As a result, the fused speed estimate is smoother than the SMESO estimate and faster than the pure Kalman filter estimate during transient operating conditions.

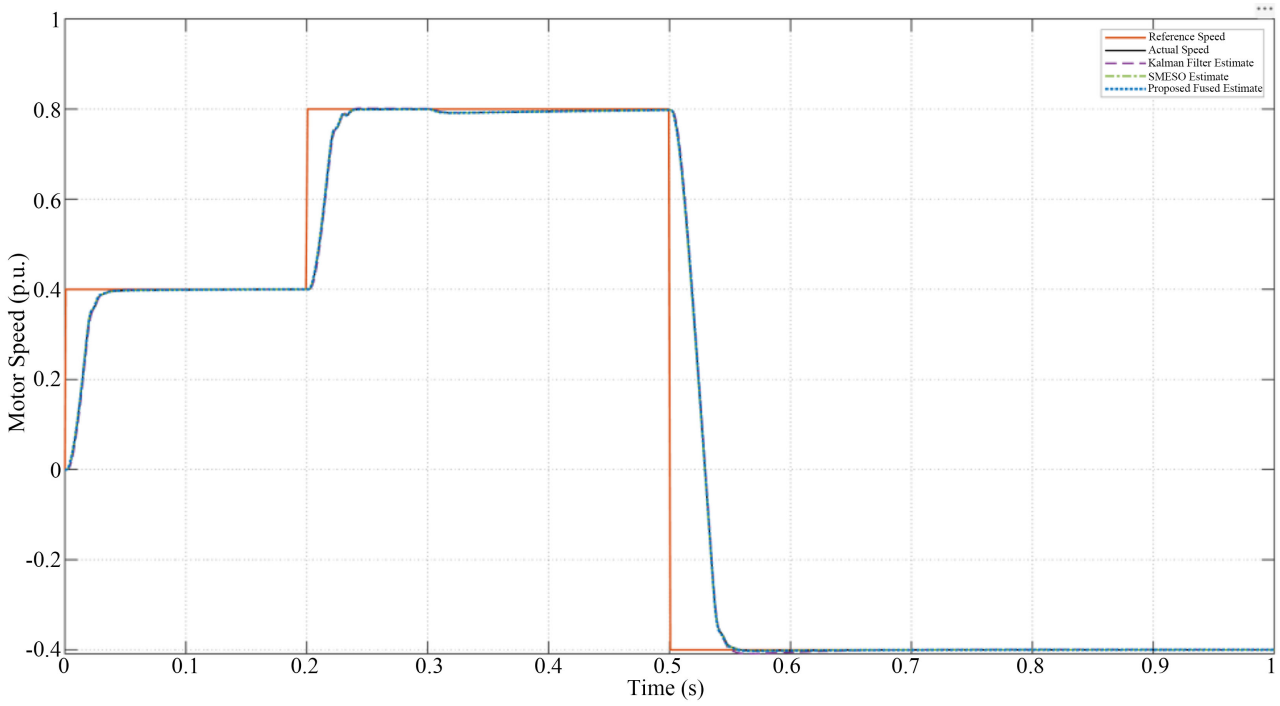

Figure 8. Speed estimation response of Kalman filter, SMESO, and proposed SMESO-Kalman fusion estimator.

Table 7 presents the quantitative comparison of the speed estimation performance. The results show that the proposed fused estimator achieves the lowest estimation error compared with the individual Kalman filter and SMESO estimators. The reduced RMSE, MAE, and maximum absolute error confirm that the fusion mechanism improves estimation accuracy and feedback reliability during both transient and steady-state operating conditions.

As per the results presented in Table 7, the suggested SMESO-Kalman estima-

tor outperforms the other types of observers in terms of estimation capabilities. Specifically, it yields lower RMSE, MAE, and maximum absolute error values compared to the pure Kalman and SMESO estimators, respectively. Moreover, the highest tracking efficiency equals 99.892%, which suggests the superiority of the fusion of the two estimators in improving estimation accuracy.

Table 7. Quantitative comparison of observer estimation performance.

Observer Architecture	RMSE	MAE	Max Absolute Error	Tracking Efficiency (%)
Pure Kalman Filter ($\hat{\omega}_{KF}$)	0.0041968	0.00207770	0.018880	99.58
Pure SMESO ($\hat{\omega}_{SMESO}$)	0.0024297	0.00083068	0.012766	99.757
Proposed Fused Estimator ($\hat{\omega}_{fused}$)	0.0010845	0.00044252	0.0060106	99.892

Figure 9 depicts the estimated load torque response for the proposed FACI-STSMC-SMESO-KF controller. It can be seen from the results that the estimated torque starts changing right after the instant when the load disturbance occurs, indicating that the observer can estimate the equivalent shaft load variation as per the Equivalent Mechanical Load model. Once the system reaches its steady-state operation, the load torque becomes bounded and equal to a stable value.

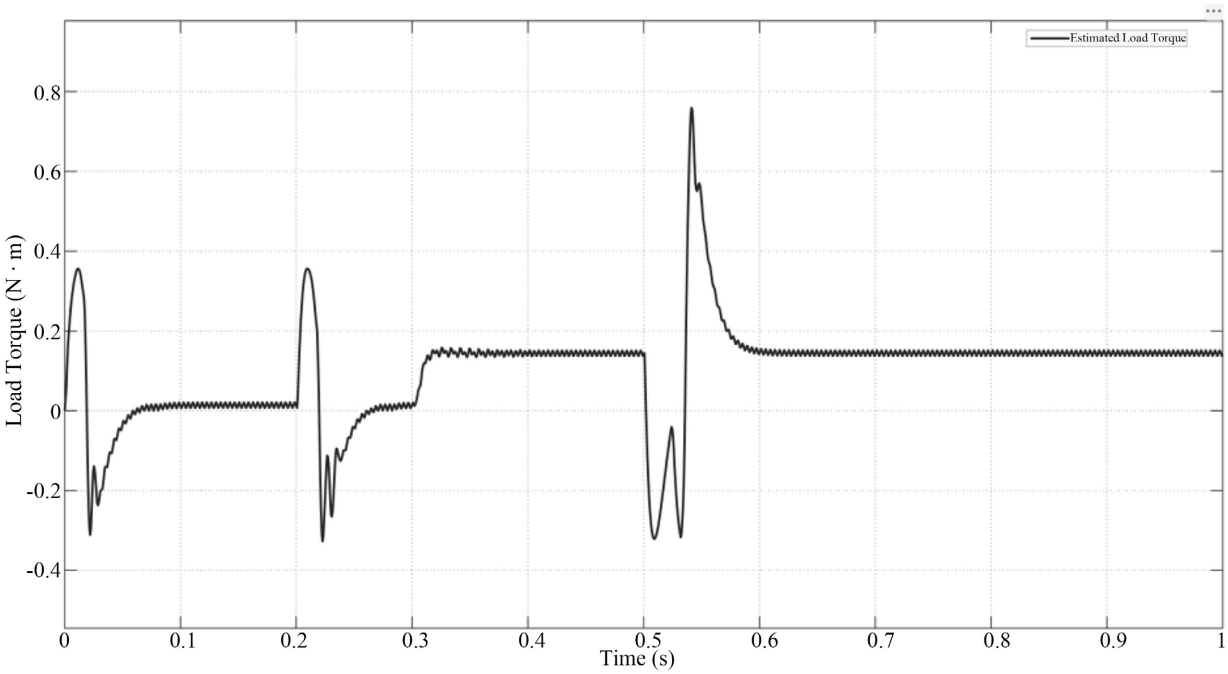

Figure 9. Estimated load torque response of the proposed FACI-STSMC-SMESO-KF controller.

4.4. Lyapunov Stability Verification

To verify the practical stability of the proposed controller, the Lyapunov candidate function defined in Section 3.6 is evaluated using the simulated sliding variable. Figure 10 shows that $V(s)$ rapidly decreases toward zero, while $\mathrm{d}V/\mathrm{d}t$ is mainly negative during the transient interval and approaches zero after settling.

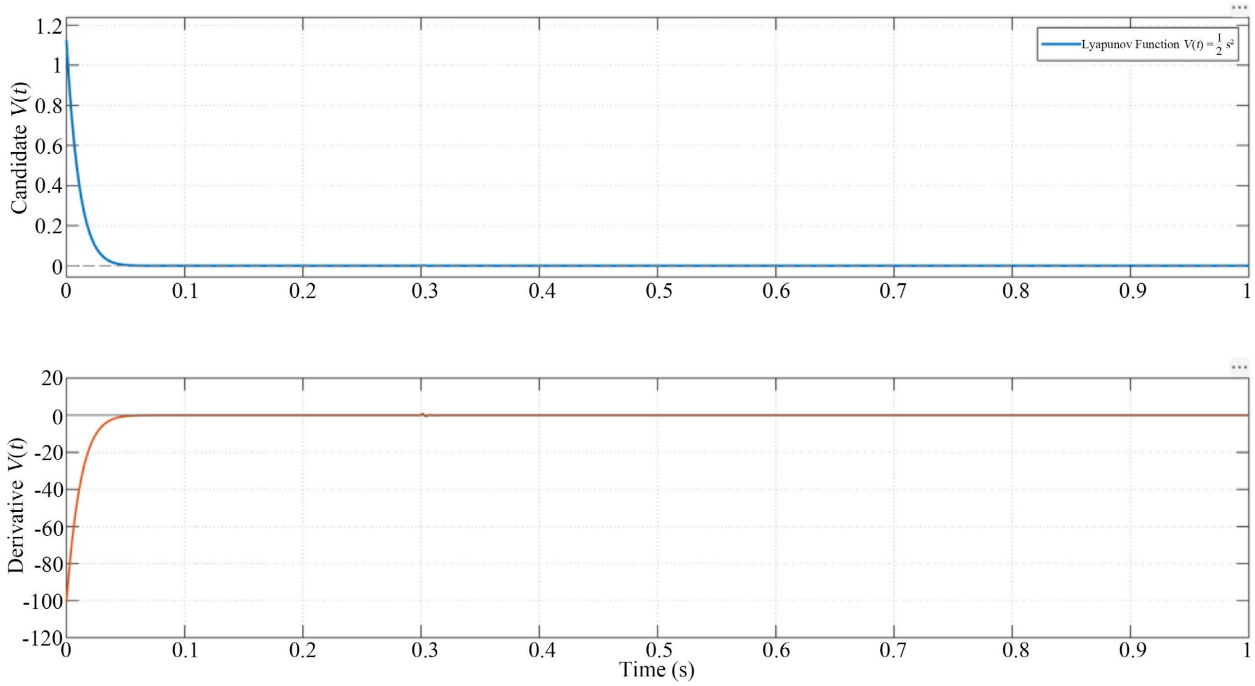

Figure 10. Lyapunov candidate function and its derivative for the proposed FACI-STSMC-SMESO-KF controller.

The rapid decay of $V(s)$ and the mainly negative behavior of $\mathrm{d}V/\mathrm{d}t$ during the transient interval confirm that the sliding variable converges toward the sliding surface and that the proposed controller maintains practical closed-loop stability.

5. Conclusion

The paper discussed a robust control strategy for SPMSM-driven electro-mechanical actuators under EMA-like disturbances. Specifically, the proposed FACI-STSMC-SMESO-KF control approach is based on the use of a conditional integral sliding mode, fuzzy adaptive super twisting, SMESO disturbance estimation, Kalman fusion, current constraint, anti-windup compensation, reverse hold-off operation, and fast recovery from loading transients. The performance of the new controller was compared with classical PI-controlled FOC and SMC in the MATLAB/Simulink simulation software. The comparison revealed enhanced speed tracking precision, lower overshoot, improved response of the q-axis currents, and better disturbance rejection of the suggested FACI-STSMC-SMESO-KF control approach. Moreover, the SMESO-Kalman fusion observer outperformed other estimators both in terms of speed accuracy and smoothness. Also, the stability of the closed-loop system was numerically validated using Lyapunov stability theory. Thus, the FACI-STSMC-SMESO-KF control approach represents an appropriate solution for controlling electro-mechanical actuator drive systems.

Acknowledgements

The author would like to acknowledge King Abdulaziz University for providing the necessary research facilities and support.

Conflicts of Interest

The authors declare no conflicts of interest regarding the publication of this paper.

References

[1] Elkholy, M.M., Algendy, M.M. and El-Hay, E.A. (2025) Modern Control Techniques and Operational Challenges in Permanent Magnet Synchronous Motors: A Comprehensive Review. *Automation*, **6**, Article 49. https://doi.org/10.3390/automation6040049

[2] Kowalski, R. and Juchmann, P. (2023) Sensorless Motor Control for Electro-Mechanical Flight Control Actuators. *CEAS Aeronautical Journal*, **14**, 1007-1018. https://doi.org/10.1007/s13272-023-00682-x

[3] Zhang, P., Shi, Z. and Yu, B. (2023) Research on Friction Compensation Method of Electromechanical Actuator Based on Improved Active Disturbance Rejection Control. *Actuators*, **12**, Article 445. https://doi.org/10.3390/act12120445

[4] Fang, Q., Zhou, Y., Ma, S., Zhang, C., Wang, Y. and Huangfu, H. (2023) Electromechanical Actuator Servo Control Technology Based on Active Disturbance Rejection Control. *Electronics*, **12**, Article 1934. https://doi.org/10.3390/electronics12081934

[5] Krause, P.C., Wasynczuk, O., Sudhoff, S.D. and Pekarek, S. (2013) Analysis of Electric Machinery and Drive Systems. 3rd Edition, Wiley-IEEE Press.

[6] Krishnan, R. (2010) Permanent Magnet Synchronous and Brushless DC Motor Drives. CRC Press.

[7] Bose, B.K. (2002) Modern Power Electronics and AC Drives. Prentice Hall.

[8] Utkin, V.I. (1992) Sliding Modes in Control and Optimization. Springer-Verlag.

[9] Levant, A. (1993) Sliding Order and Sliding Accuracy in Sliding Mode Control. *International Journal of Control*, **58**, 1247-1263. https://doi.org/10.1080/00207179308923053

[10] Levant, A. (2003) Higher-Order Sliding Modes, Differentiation and Output-Feedback Control. *International Journal of Control*, **76**, 924-941. https://doi.org/10.1080/0020717031000099029

[11] Zaihidee, F.M., Mekhilef, S. and Mubin, M. (2019) Robust Speed Control of PMSM Using Sliding Mode Control (SMC)—A Review. *Energies*, **12**, Article 1669. https://doi.org/10.3390/en12091669

[12] Liu, Y.C., Laghrouche, S., Depernet, D., Djerdir, A. and Cirrincione, M. (2021) Disturbance-Observer-Based Complementary Sliding-Mode Speed Control for PMSM Drives: A Super-Twisting Sliding-Mode Observer-Based Approach. *IEEE Journal of Emerging and Selected Topics in Power Electronics*, **9**, 5416-5428. https://doi.org/10.1109/jestpe.2020.3032103

[13] Ullah, A., Pan, J., Ullah, S. and Zhang, Z. (2024) Robust Speed Control of Permanent Magnet Synchronous Motor Drive System Using Sliding-Mode Disturbance Observer-Based Variable-Gain Fractional-Order Super-Twisting Sliding-Mode Control. *Fractal and Fractional*, **8**, Article 368. https://doi.org/10.3390/fractalfract8070368

[14] Xu, Y., Zhang, B., Kang, Y. and Wang, H. (2025) Cascaded Extended State Observer-Based Composite Sliding-Mode Controller for a PMSM Speed-Loop Anti-Interference Control Strategy. *Sensors*, **25**, Article 1133. https://doi.org/10.3390/s25041133

[15] Xie, T., Liu, Z., Zhang, Y. and Wang, J. (2023) Speed Estimation Strategy for Closed-Loop Control of Permanent Magnet Synchronous Motor Based on Kalman Filter Series Algorithm. *Electronics*, **12**, Article 4215.

[16] Wang, J., Li, Y. and Chen, X. (2025) Disturbance-Rejection Control of Permanent Magnet Synchronous Motor Based on Robust Adaptive Extended Kalman Filter. *IEICE Electronics Express*, **22**, Article 20250397.

[17] Qiao, G., Liu, G., Shi, Z., Wang, Y., Ma, S. and Lim, T.C. (2018) A Review of Electromechanical Actuators for More/All Electric Aircraft Systems. *Proceedings of the Institution of Mechanical Engineers, Part C: Journal of Mechanical Engineering Science*, **232**, 4128-4151. https://doi.org/10.1177/0954406217749869

[18] Giangrande, P., Madonna, V., Sala, G., Kladas, A., Gerada, C. and Galea, M. (2018) Design and Testing of PMSM for Aerospace EMA Applications. *IECON* 2018 44*th Annual Conference of the IEEE Industrial Electronics Society*, Washington, DC, 21-23 October 2018, 2038-2043. https://doi.org/10.1109/iecon.2018.8591318

[19] Ramamoorthy, R.T., Larimore, B. and Bhardwaj, M. (2021) Sensored Field Oriented Control of 3-Phase Permanent Magnet Synchronous Motors Using TMS320F2837x. Texas Instruments, Application Report SPRABZ0.

[20] MathWorks (2026) Field-Oriented Control of PMSM Using Hall Sensor. Motor Control Blockset Documentation. https://www.mathworks.com/help/mcb/gs/foc-pmsm-using-hall-sensor-example.html